Effect of Microstructure on Corrosion Behavior of WE43 Magnesium Alloy in As Cast and Heat-Treated Conditions

Chenxi Yang [1] ![ORCID]**, Nikhil Gupta** [2]**, Hanlin Ding** [1] **and Chongchen Xiang** [1,*] ![ORCID]

[1] Shagang School of Iron and Steel, Soochow University, 8 Jixue Road, Suzhou 215137, China; 20194249001@stu.suda.edu.cn (C.Y.); dinghanlin@suda.edu.cn (H.D.)

[2] Composite Materials and Mechanics Laboratory, Mechanical and Aerospace Engineering Department, Tandon School of Engineering, New York University, 6 MetroTech Center, Brooklyn, NY 11201, USA; ngupta@nyu.edu

[*] Correspondence: ccxiang@suda.edu.cn; Tel.: +86-152-5161-2928

Abstract: The improvement in corrosion resistance of WE43 was well realized by heat treatment. To study the influence of microstructure on the corrosion behavior of WE43 in as-cast and heat-treated conditions, an immersion test was employed with as-cast and heat-treated samples in the 3.5% NaCl solution. The corrosion rate and change of morphology were recorded and the corrosion behavior was further investigated by scanning electron microscopy (SEM). The results indicated that the corrosion rate of the WE43 alloy decreased after heat treatment. It was observed that the eutectic gradually damages the protective film on the surface of the as-cast WE43 in the process of corrosion, which further increases the corrosion rate. The Zr-rich phase formed a domed structure resulting in the adjacent area being further corroded. The Y-rich phase has little effect on the corrosion reaction.

Keywords: WE43 magnesium alloy; heat treatment; immersion test; corrosion behavior

1. Introduction

Magnesium has the preponderance of its weight as structural metal and it has the advantages of high specific strength, high specific stiffness and strong energy absorption ability, which can well meet the current trend of "lightweight". It has attracted extensive attention in automobile, 3C industry, military, aerospace and other fields [1]. In addition, magnesium alloy has good biocompatibility and can solve the problem of "stress shielding", it has a very bright prospect in the field of biomedical application [2]. However, as the most active metal among all industrial alloys, the standard electrode potential of magnesium is −2.37 V, which is about 2 V lower than that of iron and about 0.7 V lower than that of aluminum [3,4], it means that Mg alloys are prone to oxidation and corrosion in the working environment without any treatment [5]. Although Mg will form film during the process of oxidation, the improvement of corrosion resistance is extremely limited, resulting from the film being thin and not compact. The corrosion rate of Mg alloy products will be reduced by coating [6–9], alloying [10–14] and heat treatment [15,16].

WE43 contains 4 wt% Y, 3.3 wt% RE (Gd, Nd in all) and 0.5 wt% Zr. The addition of RE elements is known mainly to change the microstructure and enhance the comprehensive properties of Mg alloy attributing to the solid solution strengthening and the second phase hardening. As the solubility of Y and Gd decreases rapidly with the decline of temperature, both have prominent precipitation strengthening effects in Mg alloy. Moreover, due to the large difference between the radius of RE elements and Mg atoms, the addition of RE has a better solid solution strengthening effect compared to the addition of Al and Zn [17]. Further, the addition of Y with other elements provides a better

way to enhance the high-temperature tensile property, creep property and corrosion resistance of the Mg alloy [18]. Some studies also discovered that Y and Mg formed compounds and enriched in the direction of grain boundary to prevent further grain growth, which had the effect of refining alloy grain sizes, thus increasing the strength of the Mg-Y alloy [19]. Adding Nd is aimed at improving the performance under high temperature condition, meanwhile, the creep resistance of Mg will be enhanced to a small extent [20], while a minority of Zr includes refining the grain sizes to affect the corrosion resistance of the Mg alloy [21].

Currently, heat treatment is also considered as an effective approach to improve the properties of Mg alloy materials [22]. T5 heat treatment does not only enhance the strength by refining the grain sizes, but also provides the best plastic toughness compared to other heat treatment [23,24]. In this paper, the effect of microstructure on the corrosion behavior of the WE43 alloy in as-cast and heat-treated conditions was investigated. Corrosion rates were studied and calculated by the immersion test. The microscopies were employed to further investigate the morphology of corrosion films.

2. Materials and Methods

2.1. Material Preparation

The as-cast WE43 (Magnesium Elektron, Manchester, UK) was used in this study. The composition of WE43 used in this article is shown in Table 1. In order to acquire the heat-treated WE43, a portion of the as-cast WE43 was cut and first hot rolled on a reversing mill at 525 °C, then artificially aged at 210 °C for 48 h to achieve the peak aged—hereinafter referred to as WE43-T5.

Table 1. The chemical composition of WE43.

Element	Yttrium	Rare Earths	Zirconium	Magnesium
Proportion (%)	4.3	3.4	0.4	Balance

The as-cast WE43 and WE43-T5 were machined into $20 \times 50 \times 2$ mm^3 for the following experiments. The surface of all samples had been polished down to 1 μm with water-based diamond suspensions and ended in cleaning with acetone and drying in air.

2.2. Immersion Test

In total, 3.5% sodium chloride (NaCl) solution was prepared to simulate the seawater environment for the immersion test and then the balance (AE160, METTLER TOLEDO, Zurich, Switzerland), which has a weighting range from 0 to 162 g and whose readability is 0.1 mg, is used to get the samples' weights. We put a round piece of paper on the pan in the balance and pressed the control bar to blank out the display, getting the "0.0000" on the screen. Following that, the as-cast WE43 and WE43-T5 are, respectively, put into the balance and their initial weight is obtained by reading the value on the screen. Test samples were cleaned by distilled water and dried after taking out the solution. The cleaned samples were then submerged in chromate acid (200 g/dm^3 CrO$_3$ + 10 g/dm^3 AgNO$_3$) to remove corrosion products. Subsequently, distilled water was used again to clean the surface of samples, followed by rinsing with acetone and desiccation. The weight of these processed samples was recorded. The values between the initial weight and the weight after immersion were calculated, which indicated weight loss during the corrosion. The corrosion rate and weight loss were calculated by applying the following equations.

$$V = (m_0 - m_t)/(S \cdot t) \tag{1}$$

$$W = ((m_0 - m_t)/m_0) * 100\% \tag{2}$$

where V denotes the corrosion rate and W represents the weight loss on the left side of the formula. m_0 denotes the initial weight, S denotes the surface area of each sample (1000 mm^3 in this paper) and t represents the corrosion days of samples.

2.3. Microstructure Characterization

Before observing the initial microstructure, sequential polishing is needed with up to 1 μm diamond slurry and etching with Nital etchant containing 5% nitric acid. The corroded samples are directly observed after the procedures before weighing which is mentioned in the immersion test. The microstructures of the as-cast WE43 and WE43-T5 were observed via a scanning electron microscope (Hitachi S-3400N, Hitachi, Tokyo, Japan) and optical microscope (Nikon Epiphot 200, Nikon, Tokyo, Japan) equipped with a live camera. Energy dispersive spectroscopy (EDS, EDAX Inc., Mahwah, NJ, USA) was used to obtain the spectrum of phases.

3. Results

3.1. The Initial Microstructure of As-Cast WE43 and WE43-T5

As shown in Figure 1a, as-cast WE43 is made up primarily of bulk α-Mg and irregular eutectic formed along the grain boundary. However, eutectic was dissolved into the matrix after heat treatment as shown in Figure 1b. The grain sizes of as-cast WE43 and WE43-T5 were measured as 54.1 ± 18.6 μm and 24.8 ± 12.5 μm, respectively. Further observation of microstructure by EDS indicated that eutectic contains the element of Y, Nd, and Gd in addition to Mg. It has also been documented that the chemical composition of this eutectic region is mainly $Mg_{24}RE_5$ in a recent study [25,26].

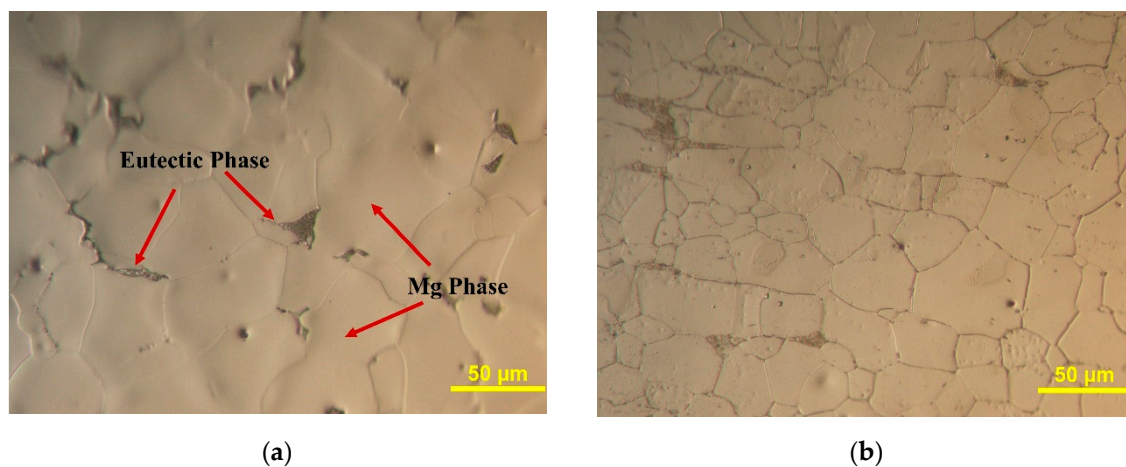| (a) | (b) |

Figure 1. The optical microscopy images of WE43 in (**a**) as-cast (**b**) T5 condition.

There are other categories of precipitated phases in both as-cast WE43 and WE43-T5 which are identified as the Y-rich phase and the Zr-rich phase [27]. The Y-rich phase has a regular shape with a small size of about 1 μm and mainly exists around eutectic in as-cast WE43, while in WE43-T5, Y-rich phases are mostly distributed on the grain boundary of the matrix. In addition, the Zr-rich phase is relatively irregular in shape and distributes randomly in the matrix. The eutectic phase and the Y-rich phase have been identified as $Mg_{24}RE_5$ phase and β-$Mg_{14}Nd_2Y$ phase; detailed morphology and EDS spectrums of these phases can be found in our previous study [27,28].

3.2. Corrosion Behavior

Both as-cast WE43 and WE43-T5 samples were prepared for the immersion test with a 3.5% NaCl solution to investigate the corrosion behavior. As the immersion time increases, WE43 in two conditions exhibited quite different corrosion behaviors. The comparison in Figure 2a,b showed the

different corrosion rates and weight loss between as-cast WE43 and WE43-T5 samples. It was observed that the corrosion rate of as-cast WE43 maintained an upward trend over time and finally reached 3.64 ± 0.81 mg·cm^{-2}·day^{-1}. On the contrary, the corrosion rate of WE43-T5 remained unchanged and reached 0.88 ± 0.14 mg·cm^{-2}·day^{-1} on the 7th day. Figure 2b showed the comparative data of weight loss between two conditions after immersion. The weight loss of both samples was quite close before the 4th day while the weight loss of as-cast WE43 changed dramatically and increased at the beginning of the 5th day. Compared to that, the weight loss of WE43-T5 increases slowly during the test.
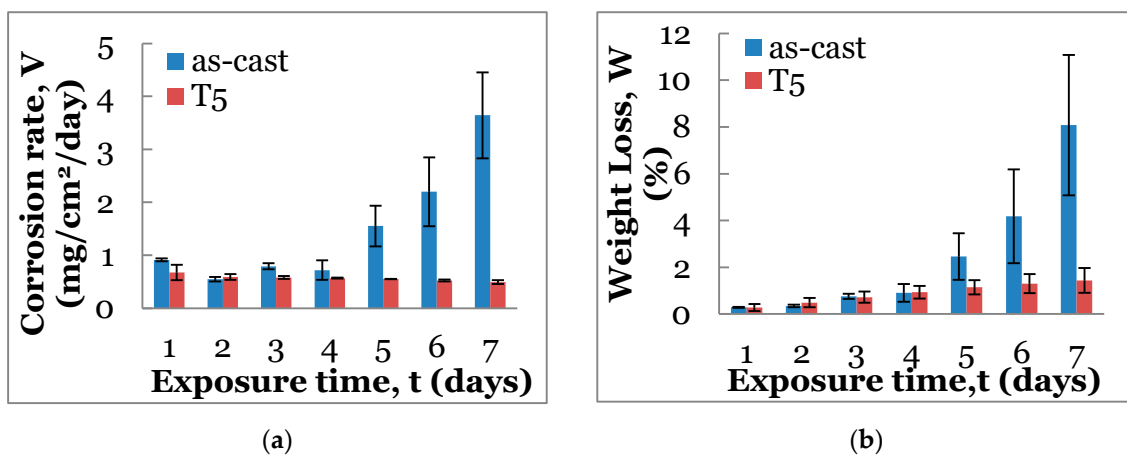

(a) 　　　　　　　　　　　　　　　　　　　　　(b)

Figure 2. Comparison of (**a**) corrosion rates and (**b**) weight loss.

The macro morphology of as-cast WE43 and WE43-T5 after 7 days of corrosion is displayed in Figures 3 and 4. Severe damage occurred on the as-cast WE43, while WE43-T5 exhibited integrity appearance without localized corrosion characteristic after 7 days' immersion.
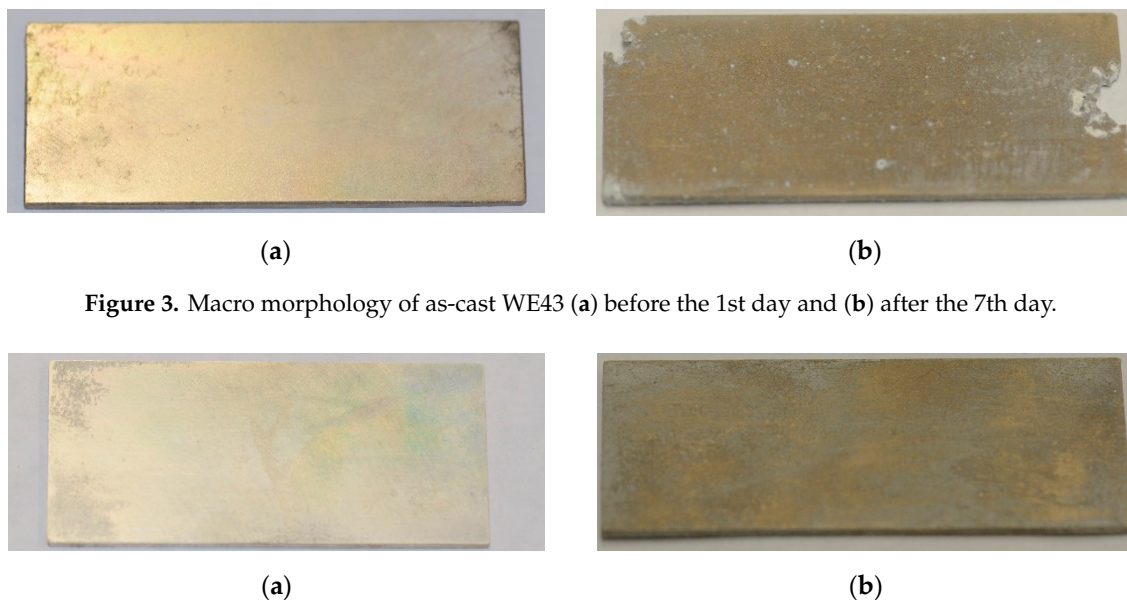

(a) 　　　　　　　　　　　　　　　　　　　　　(b)

Figure 3. Macro morphology of as-cast WE43 (**a**) before the 1st day and (**b**) after the 7th day.

(a) 　　　　　　　　　　　　　　　　　　　　　(b)

Figure 4. Macro morphology of WE43-T5 (**a**) before the 1st day and (**b**) after the 7th day.

Optical microscopy was used to investigate the further appearance of the sample. As shown in Figure 5, the multiple external pitting corrosion pits in as-cast WE43 signified that the specimen was heavily corroded. On the other hand, only light pits had an appearance in WE43-T5 which is shown in Figure 6. Hydrogen bubbles were observed on the surfaces of all samples during the test. The bubbles grew up gradually until they reached a critical size or specific external factors were involved in the

solution. Then, new hydrogen bubbles tended to form at the same locations and there remained some white dots which are considered to be reaction products on the surface.
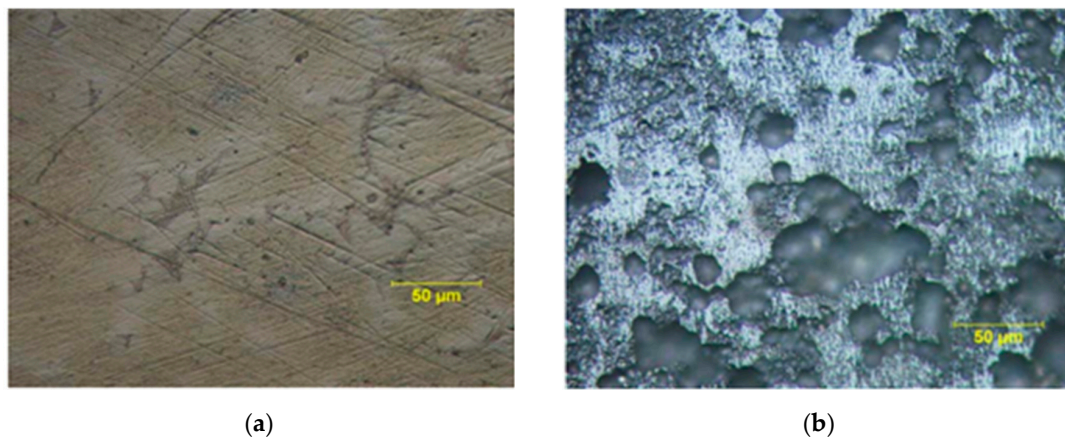

Figure 5. Optical microscopy images of as-cast WE43 (**a**) before the 1st day and (**b**) after the 7th day.
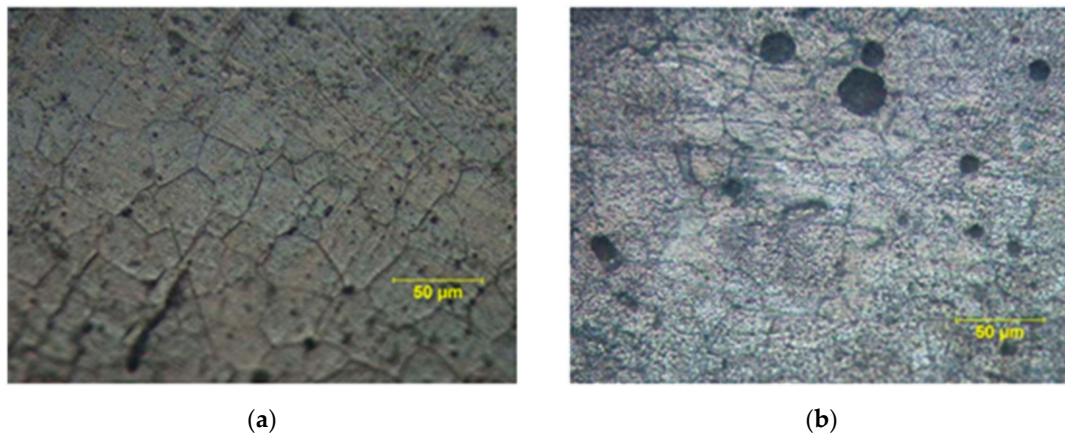

Figure 6. Optical microscopy images of WE43-T5 (**a**) before the 1st day and (**b**) after the 7th day.

Scanning electron microscopy was employed to achieve a detailed corrosion morphology of the sample. As shown in Figure 7a,b, it is apparent that the corroded pits existing in WE43-T5 are smaller than that of as-cast WE43, and the magnitude of pits for as-cast WE43 and WE43-T5 are 1 mm and 0.01 mm, respectively.
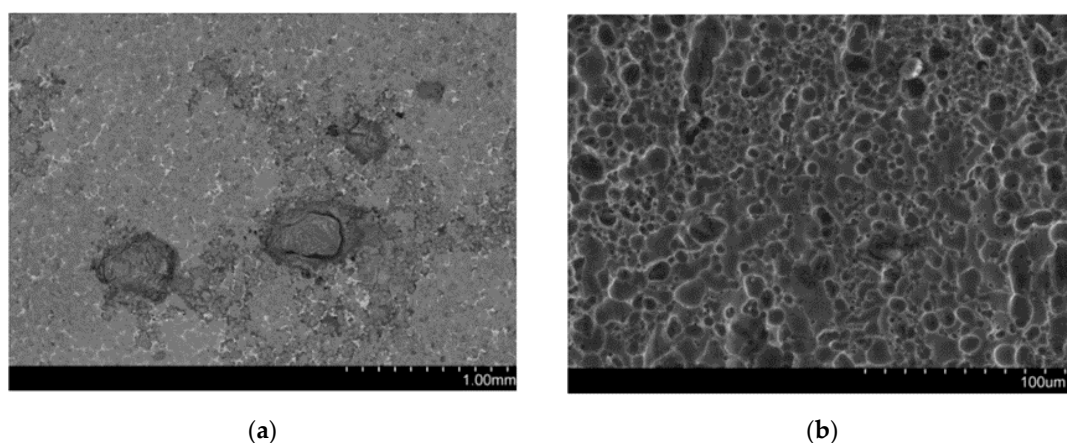

Figure 7. SEM images of pitting corrosion of WE43 in (**a**) as-cast and (**b**) T5 condition after immersion test.

4. Discussion

The Mg alloy will form two corrosion films on the surface during the process of corrosion which is identified as MgO and Mg (OH)$_2$ in the former paper [14,29]. At the outset, the MgO layer formed on the surface of the Mg alloy on account of anodic oxidation, followed by the hydration of the oxide layer, the magnesium hydroxide (Mg (OH)$_2$) layer appeared and finally formed two layers of corrosion film. However, because of the porosity of both the two corrosion films [30], they have a weak effect on resisting external corrosion. Afterwards, although the corrosion films can slow down the corrosion reactions for as-cast WE43 and WE43-T5, the NaCl solution can still penetrate the layers easily. According to former research, which used an isotopic tracer, about the growth of corrosion film on Mg alloys [31], the transportation of oxygen and inward diffusion of hydrogen-dominated film growth compared with outward diffusion of Mg.

Pitting corrosion morphology occurred to different degrees in the as-cast WE43 and WE43-T5 samples. The size of the corrosion pits has a significant decrease after heat treatment which was from 1 mm to 10 μm, as shown in Figure 7a,b. It indicated that the pitting corrosion is harder to form in WE43-T5, in other words, the corrosion resistance had greatly improved on account of heat treatment. It had been previously reported that the concentration of chloride and pH value in solutions should answer for the corrosion on Mg and its alloys [32,33]. That low pH value environment tends to bring about localized corrosion while the WE43 alloy is more prone to uniform corrosion under high pH value (10.5). Przondziono et al. also observed similar localized pitting corrosion morphology by changing Cl concentration [15]. In addition, Wu L and Li H found that the protective films that took shape on the surface would be penetrated by Cl$^-$ as time went by; then, a large number of pits would be left on the film which are thought of as activation centers of corrosion reaction [34].

It is also shown in Figure 1 that heat treatment has a positive effect on reducing the grain size of WE43 and the eutectic dissolved in the matrix after T5 heat treatment. Typically, increased grain boundaries lead to more prone to corrosion because the impurity atoms which are in unstable states prefer to be enriched at the grain boundary [35]. However, it was evident that WE43-T5, which has a smaller grain size, has better corrosion resistance than as-cast WE43. This may be contributed by the atomic flow being enhanced with the increase in grain boundaries counteracting the stress and making it better for the oxide layer to adhere to a substrate in turn, thus improving the corrosion resistance [11,36].

As shown in Figure 8, the domes were observed around the Zr-rich phases in both as-cast WE43 and WE43-T5 samples. The existence of these domes has been mentioned in the corrosion process from different Mg alloys [32,37,38]. It is reported that impurity elements, such as Ni, Cr, Zr, and Fe, tend to induce a smaller galvanic effect than other phases on account of their high Volta potential difference regarding the Mg matrix [38,39]. Compared to other phases, Zr-rich particles have the highest Volta potential values [38], as shown in Table 2. Hence, the Zr-rich particles here functioned as local cathodes. Mg matrix around them was gradually corroded as anode and hydrogen evolution occurs in these regions. The cathodic reaction is as follows:

$$2H_2O + 2e^- \rightarrow 2OH^- + H_2 \uparrow \tag{3}$$

Table 2. Volta potential differences of the phases, data from [38].

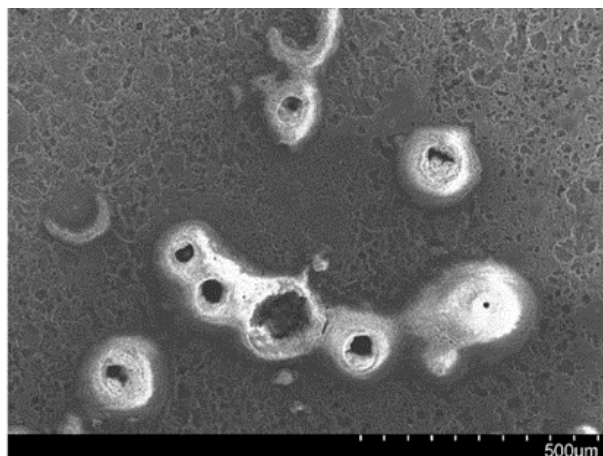| Phases	Zr-Rich	Y-Rich	Eutectic
ΔV(mV)	+170 ± 10	+50 ± 10	+25 ± 5

Figure 8. SEM images of hemisphere domes appeared on WE43.

Therefore, in the corrosion process, the dome-shaped structure was formed on the Zr-rich phase first. Then, due to the generation of hydroxide ions, the pH value near the Zr-rich phase increases, making it easier to form Mg (OH)$_2$ protective film in this region. However, the corrosion reaction will continue even after the domed shell is formed because both corrosion products and protective films have a porous structure. The schematic illustration of the Zr-rich phase region is shown in Figure 9. A galvanic cell is formed in this region owing to the large potential difference between the Zr-rich phase and the Mg matrix. Among them, the hydroxide ions and hydrogen were separated from H$_2$O molecules near the Zr-rich phase. The increase in hydroxide ions makes the MgO on the Zr-rich phase more prone to hydration reaction, which makes the MgO layer thinner, while the Mg (OH)$_2$ corrosion layer thickens sharply. Although the two layers of corrosion film have the character of porosity and low density, they still can prevent the corrosion solution from further contact with WE43 to a certain degree. The region slightly away from the Zr-rich phase experienced a serious cathodic reaction, in terms of a difference between the potential of Zr-rich and α-Mg, which accelerated the corrosion rate in this region. Moreover, due to the increase in pH value around the Zr-rich phase, corrosion pits are not easy to form in this region [15,32]. Therefore, electrochemical corrosion occurs only near the Zr-rich phase, without the local pitting phenomenon.
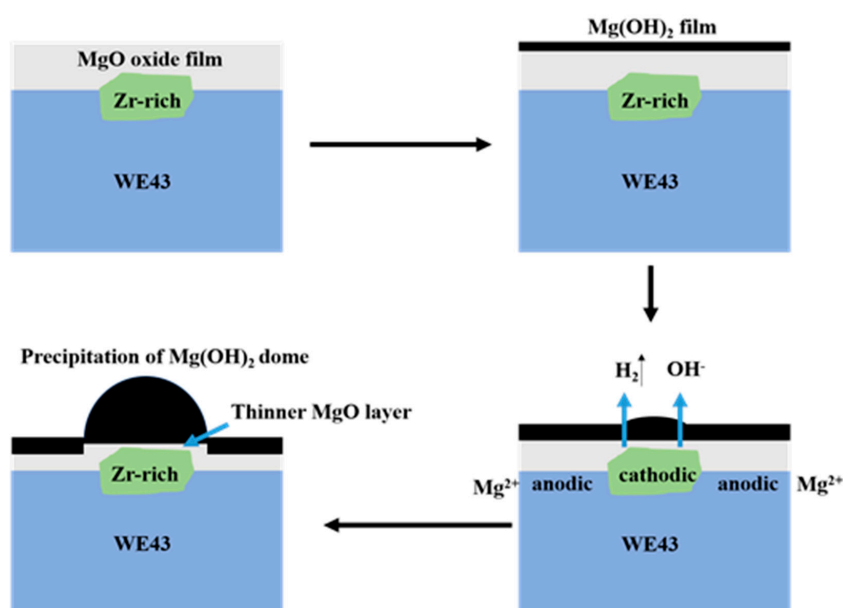

Figure 9. Schematic illustration for the effect of Zr-rich phase on corrosion behavior.

It is reported in the previous study [28] that the Y-rich phase is the small square particle which just has a size of 1 μm. When in the as-cast WE43, the Y-rich phase has a presence in the eutectic, and after heat treatment, the eutectic dissolves into the matrix, while the Y-rich phase remains in the Mg matrix due to their high melting point. As shown in Figure 10, it was found that there was some pitting corrosion around the Y-rich phase on both as-cast WE43 and WE43-T5 samples. It is known from the literature [38] that there is a minimal potential difference between the Y-rich phase and α-Mg. Unlike the Zr-rich phase, the electrochemical corrosion around the Y-rich phase and the pH value will not rise significantly. Therefore, local pitting corrosion and electrochemical corrosion coexist near the Y-rich phase. In addition, when the matrix near the Y-rich phase gradually corroded, the Y-rich phase was still embedded in the matrix due to the high corrosion resistance of the Y-rich phase itself until all nearby substrates were corroded and washed off together in the subsequent treatment of corrosion products. The schematic illustration for the effect of the Y-rich phase is shown in Figure 11.
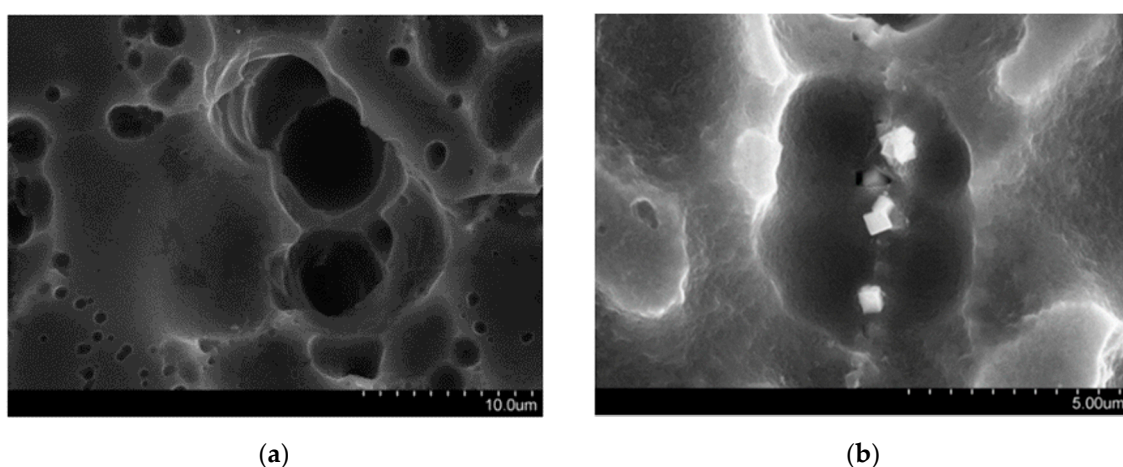

(a)   (b)

Figure 10. SEM images of corrosion pits (**a**) without visible Y-rich phases and (**b**) with visible Y-rich phases.
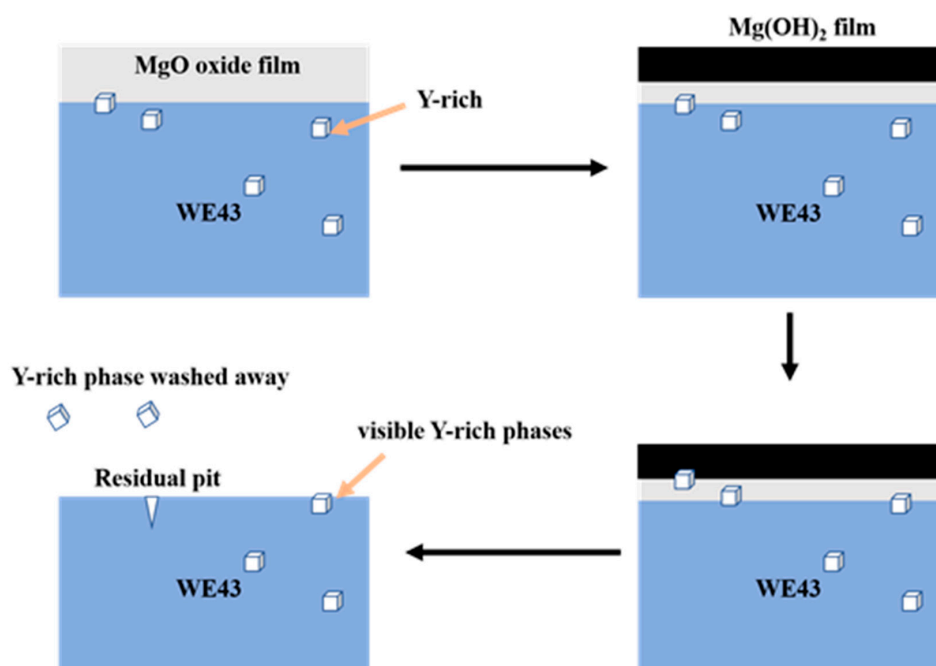

Figure 11. Schematic illustration for the effect of Y-rich phase on corrosion behavior.

There are many irregular sharp and discontinuous eutectic in the as-cast WE43. The eutectic phase has a low potential difference regarding the α-Mg matrix which is similar to the Y-rich phase. However, unlike the Y-rich phase, the eutectic occupies a large area and is embedded in the matrix. Figure 12 showed the SEM images of eutectic in as-cast WE43 after corrosion, the white part is convex eutectic and the black part is the concave matrix. The α-Mg matrix near the eutectic turned to the MgO and Mg $(OH)_2$ layer gradually by corrosion, while eutectic does not change significantly for its resistance of corrosion. Hence, near the upper part of the eutectic is full of corrosion products, then the corrosion films fall off after immersing in chromate acid, leaving the outstanding eutectic and uncorroded α-Mg. At the first stage of the corrosion process, the corrosion layers are continuously forming on the surface of the α-Mg matrix. The eutectic can enter the MgO corrosion layer at this time because of its high stability, just like the Y-rich phase. At this stage, the eutectic phase does not have much influence on the corrosion behavior of the WE43 alloy. Therefore, the corrosion velocity and mass loss of WE43 in two conditions are almost the same initially as shown in Figure 2a,b. With the further corrosion of the matrix, the eutectic phase can still maintain its original shape and start to damage the protective film. As the corrosion proceeds, the eutectic phase achieves the breakthrough of bi-layers finally. Li reported a similar corrosion model that the long period stacking ordered (LPSO) phase will damage the film to expedite the corrosion [40]. Unlike the Y-rich phase, the eutectic experiences difficulty falling off since it is firmly embedded in the matrix, which leads to the corrosion films around the eutectic suffering serious damage. The solution is in direct contact with the surface through cracks of matrix and eutectic, accelerating the corrosion rate eventually. A diagram of the eutectic is shown in Figure 13.
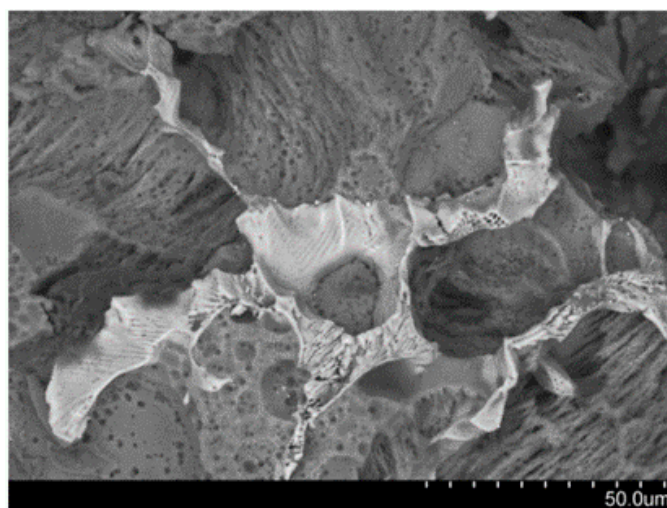

Figure 12. SEM image of the eutectic region on the surface of as-cast WE43 alloy after corrosion.

It is worth noticing that the largest size of eutectic or particle should highly depend on the thickness of the corrosion layer of the alloy since it may punch through and damage the layer. The thickness of the corrosion layer was found to be 27.2 to 62.9 μm for the as-cast WE43 and around 10 μm for the heat-treated alloy, respectively [41,42]. Therefore, the largest size of the eutectic or particle that would damage the corrosion layer and affect the corrosion behavior should be 27 μm for the untreated WE43 and 10 μm for the heat-treated WE43.
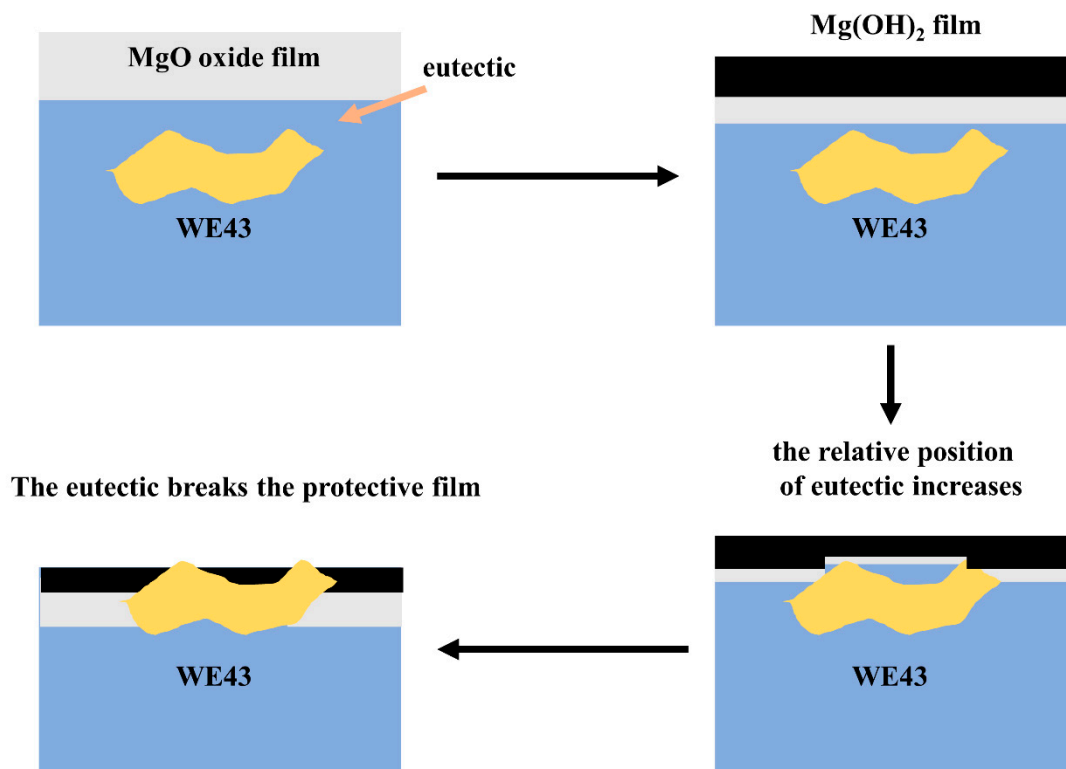
Figure 13. Schematic illustration for the effect of eutectic on corrosion behavior.

5. Conclusions

The corrosion behavior of as-cast WE43 and WE43-T5 was investigated by employing the immersion test in the 3.5 wt% NaCl solution. The corrosion resistance of as-cast WE43 and WE43-T5 were evaluated by corrosion rate and mass loss. The effect of each precipitate on the corrosion films of WE43 and the improvement of its corrosion behavior is emphatically studied. The results are as follows.

(1) For the as-cast WE43 alloy, the eutectic dissolved after T5 heat treatment and the grain size decreased significantly from 54.1 ± 18.6 to 24.8 ± 12.5 μm. However, T5 heat treatment did not dissolve the second phase.

(2) The corrosion rate and mass loss of as-cast WE43 and WE43-T5 were the same at the beginning of corrosion, while the corrosion reaction in as-cast WE43 increased rapidly after the 4th day, reaching 3.64 ± 0.81 mg·cm^{-2}·day^{-1} on the 7th day. On the contrary, the corrosion rate of WE43-T5 did not change much.

(3) The hemispheric dome structure formed above the Zr-rich phase was ascribed to the large potential difference between the Zr-rich phase and the α-Mg matrix. On the one hand, the cathodic reaction occurs in the Zr-rich phase, which generates more hydroxide and increases the pH value, thus producing more Mg (OH)$_2$ corrosion films, which alleviates the corrosion rate of WE43 to some extent. On the other hand, the anodic reaction occurs far away from the Zr-rich phase, which accelerated the corrosion rate. In general, the Zr-rich phase has a negative effect on slowing down the corrosion reaction. The Y-rich phase, identified as β-Mg$_{14}$Nd$_2$Y, is quite small compared to other phases and has an insignificant influence on corrosion behavior, and a certain amount of the Y-rich phase is found near pitting corrosion. The eutectic, which was identified as Mg$_{24}$RE$_5$ in our previous study, is large and has irregular sharp morphology leading to a significant increase in the corrosion rate. It is noted that whether the size of the eutectic phase affects the corrosion rate is linked to the thickness of the corrosion layer, and the critical size for damaging the integrity of the films on the surface of untreated WE43 and WE4-T5 should be 27 μm and 10 μm, respectively.

References

1. Xu, T.; Yang, Y.; Peng, X.; Song, J.; Pan, F. Overview of advancement and development trend on magnesium alloy. *J. Magnes. Alloys* **2019**, *7*, 536–544. [CrossRef]

2. Chen, Y.; Xu, Z.; Smith, C.; Sankar, J. Recent advances on the development of magnesium alloys for biodegradable implants. *Acta Biomater.* **2014**, *10*, 4561–4573. [CrossRef]

3. Song, G.L.; Atrens, A. Corrosion Mechanisms of Magnesium Alloys. *Adv. Eng. Mater.* **1999**, *1*, 11–33. [CrossRef]

4. Ghali, E.; Dietzel, W.; Kainer, K.-U. General and Localized Corrosion of Magnesium Alloys: A Critical Review. *J. Mater. Eng. Perform.* **2004**, *13*, 7–23. [CrossRef]

5. Mordike, B.L.; Ebert, T. Magnesium: Properties—Applications—Potential. *Mater. Sci. Eng. A* **2001**, *302*, 37–45. [CrossRef]

6. Zai, W.; Zhang, X.; Su, Y.; Man, H.; Li, G.; Lian, J. Comparison of corrosion resistance and biocompatibility of magnesium phosphate (MgP), zinc phosphate (ZnP) and calcium phosphate (CaP) conversion coatings on Mg alloy. *Surf. Coat. Technol.* **2020**, *397*, 125919. [CrossRef]

7. Song, G. Recent Progress in Corrosion and Protection of Magnesium Alloys. *Adv. Eng. Mater.* **2005**, *7*, 563–586. [CrossRef]

8. Wang, X.; Xiaopeng, L.; Ju, P.; Chen, Y.; Zhang, T.; Wang, F. Thermal control property and corrosion resistance of PEO coatings on AZ91 Mg alloy. *Surf. Coat. Technol.* **2020**, *393*, 125709. [CrossRef]

9. Wang, H.; Yu, B.; Wang, W.; Ren, G.; Liang, W.; Zhang, J. Improved corrosion resistance of AZ91D magnesium alloy by a zinc–yttrium coating. *J. Alloys Compd.* **2014**, *582*, 457–460. [CrossRef]

10. Karakulak, E. A review: Past, present and future of grain refining of magnesium castings. *J. Magnes. Alloys* **2019**, *7*, 355–369. [CrossRef]

11. Wan, Y.; Xu, S.; Liu, C.; Gao, Y.; Jiang, S.N.; Chen, Z. Enhanced strength and corrosion resistance of Mg-Gd-Y-Zr alloy with ultrafine grains. *Mater. Lett.* **2018**, *213*, 274–277. [CrossRef]

12. Zhang, C.; Wu, L.; Liu, H.; Huang, G.; Jiang, B.; Atrens, A.; Pan, F. Microstructure and corrosion behavior of Mg-Sc binary alloys in 3.5 wt.% NaCl solution. *Corros. Sci.* **2020**, *174*, 108831. [CrossRef]

13. Liu, Y.; Cheng, W.; Liu, Y.-H.; Niu, X.-F.; Wang, H.-X.; Wang, L.-F.; Cui, Z.-Q. Effect of alloyed Ca on the microstructure and corrosion behavior of extruded Mg-Bi-Al-based alloys. *Mater. Charact.* **2020**, *163*, 110292. [CrossRef]

14. Sun, Y.; Wang, R.; Peng, C.; Xiao-Feng, W. Microstructure and corrosion behavior of as-homogenized Mg-xLi-3Al-2Zn-0.2Zr alloys (x = 5, 8, 11 wt%). *Mater. Charact.* **2020**, *159*, 110031. [CrossRef]

15. Przondziono, J.; Walke, W.; Hadasik, E.; Szala, J.; Wieczorek, J. Corrosion resistance tests of magnesium alloy WE43 after extrusion. *Metalurgija* **2013**, *52*, 243–246.

16. Sun, Y.; Wang, R.; Peng, C.; Zhang, C. Microstructure and corrosion behavior of as-extruded Mg-xLi-3Al-2Zn-0.2Zr alloys (x = 5, 8, 11 wt.%). *Corros. Sci.* **2020**, *167*, 108487. [CrossRef]

17. Gao, L.; Chen, R.; Han, E. Effects of rare-earth elements Gd and Y on the solid solution strengthening of Mg alloys. *J. Alloys Compd.* **2009**, *481*, 379–384. [CrossRef]

18. Huang, S.; Wang, J.; Hou, F.; Huang, X.; Pan, F. Effect of Gd and Y contents on the microstructural evolution of long period stacking ordered phase and the corresponding mechanical properties in Mg–Gd–Y–Zn–Mn alloys. *Mater. Sci. Eng. A* **2014**, *612*, 363–370. [CrossRef]

19. Peng, Q.; Wang, J.; Wu, Y.; Wang, L. Microstructures and tensile properties of Mg–8Gd–0.6Zr–xNd–yY (x + y = 3, mass%) alloys. *Mater. Sci. Eng. A* **2006**, *433*, 133–138. [CrossRef]

20. Yan, J.; Sun, Y.; Xue, F.; Xue, S.; Tao, W. Microstructure and mechanical properties in cast magnesium–neodymium binary alloys. *Mater. Sci. Eng. A* **2008**, *476*, 366–371. [CrossRef]

21. He, S.; Zeng, X.; Peng, L.; Gao, X.; Nie, J.; Ding, W. Precipitation in a Mg–10Gd–3Y–0.4Zr (wt.%) alloy during isothermal ageing at 250 °C. *J. Alloys Compd.* **2006**, *421*, 309–313. [CrossRef]

22. Riontino, G.; Massazza, M.; Lussana, D.; Mengucci, P.; Barucca, G.; Ferragut, R. A novel thermal treatment on a Mg–4.2Y–2.3Nd–0.6Zr (WE43) alloy. *Mater. Sci. Eng. A* **2008**, *494*, 445–448. [CrossRef]

23. Bhattacharyya, J.; Wang, F.; McQuade, P.; Agnew, S. Deformation and fracture behavior of Mg alloy, WE43, after various aging heat treatments. *Mater. Sci. Eng. A* **2017**, *705*, 79–88. [CrossRef]

24. Ghorbanpour, S.; McWilliams, B.A.; Knezevic, M. Effect of hot working and aging heat treatments on monotonic, cyclic, and fatigue behavior of WE43 magnesium alloy. *Mater. Sci. Eng. A* **2019**, *747*, 27–41. [CrossRef]

25. Nie, J.F. Precipitation and Hardening in Magnesium Alloys. *Met. Mater. Trans. A* **2012**, *43*, 3891–3939. [CrossRef]

26. Milkereit, B.; Burgschat, L.; Kemsies, R.H.; Springer, A.; Schick, C.; Kessler, O. In situ differential scanning calorimetry analysis of dissolution and precipitation kinetics in Mg–Y–RE alloy WE43. *J. Magnes. Alloys* **2019**, *7*, 1–14. [CrossRef]

27. Tian, Z.; Yang, Q.; Guan, K.; Meng, J.; Cao, Z. Microstructure and mechanical properties of a peak-aged Mg-5Y-2.5Nd-1.5Gd-0.5Zr casting alloy. *J. Alloys Compd.* **2018**, *731*, 704–713. [CrossRef]

28. Xiang, C.; Gupta, N.; Coelho, P.; Cho, K. Effect of microstructure on tensile and compressive behavior of WE43 alloy in as cast and heat treated conditions. *Mater. Sci. Eng. A* **2018**, *710*, 74–85. [CrossRef]

29. Taheri, M.; Danaie, M.; Kish, J.R. TEM Examination of the Film Formed on Corroding Mg Prior to Breakdown. *J. Electrochem. Soc.* **2014**, *161*, C89–C94. [CrossRef]

30. Brady, M.P.; Rother, G.; Anovitz, L.M.; Littrell, K.C.; Unocic, K.A.; Elsentriecy, H.H.; Song, G.-L.; Thomson, J.K.; Gallego, N.C.; Davis, B.G. Film Breakdown and Nano-Porous Mg(OH)2Formation from Corrosion of Magnesium Alloys in Salt Solutions. *J. Electrochem. Soc.* **2015**, *162*, C140–C149. [CrossRef]

31. Brady, M.P.; Fayek, M.; Elsentriecy, H.H.; Unocic, K.A.; Anovitz, L.M.; Keiser, J.R.; Song, G.L.; Davis, B. Tracer Film Growth Study of Hydrogen and Oxygen from the Corrosion of Magnesium in Water. *J. Electrochem. Soc.* **2014**, *161*, C395–C404. [CrossRef]

32. Chu, P.-W.; Marquis, E.A. Linking the microstructure of a heat-treated WE43 Mg alloy with its corrosion behavior. *Corros. Sci.* **2015**, *101*, 94–104. [CrossRef]

33. Williams, G.; McMurray, H.N.; Birbilis, N. Controlling factors in localised corrosion morphologies observed for magnesium immersed in chloride containing electrolyte. *Faraday Discuss.* **2015**, *180*, 313–330. [CrossRef] [PubMed]

34. Wu, L.; Li, H. Effect of selective oxidation on corrosion behavior of Mg–Gd–Y–Zn–Zr alloy. *Corros. Sci.* **2018**, *142*, 238–248. [CrossRef]

35. Metalnikov, P.; Ben-Hamu, G.; Templeman, Y.; Shin, K.S.; Meshi, L. The relation between Mn additions, microstructure and corrosion behavior of new wrought Mg-5Al alloys. *Mater. Charact.* **2018**, *145*, 101–115. [CrossRef]

36. Huo, W.; Zhang, W.; Lu, J.; Zhang, Y. Simultaneously enhanced strength and corrosion resistance of Mg–3Al–1Zn alloy sheets with nano-grained surface layer produced by sliding friction treatment. *J. Alloys Compd.* **2017**, *720*, 324–331. [CrossRef]

37. Danaie, M.; Asmussen, R.M.; Jakupi, P.; Shoesmith, D.W.; Botton, G.A. The cathodic behaviour of Al–Mn precipitates during atmospheric and saline aqueous corrosion of a sand-cast AM50 alloy. *Corros. Sci.* **2014**, *83*, 299–309. [CrossRef]

38. Coy, A.; Viejo, F.; Skeldon, P.; Thompson, G. Susceptibility of rare-earth-magnesium alloys to micro-galvanic corrosion. *Corros. Sci.* **2010**, *52*, 3896–3906. [CrossRef]

39. Yang, L.; Zhou, X.; Liang, S.-M.; Schmid-Fetzer, R.; Fan, Z.; Scamans, G.; Robson, J.; Thompson, G.E. Effect of traces of silicon on the formation of Fe-rich particles in pure magnesium and the corrosion susceptibility of magnesium. *J. Alloys Compd.* **2015**, *619*, 396–400. [CrossRef]

40. Li, C.; Xu, D.; Zeng, Z.; Wang, B.; Sheng, L.; Chen, X.-B.; Han, E.-H. Effect of volume fraction of LPSO phases on corrosion and mechanical properties of Mg-Zn-Y alloys. *Mater. Des.* **2017**, *121*, 430–441. [CrossRef]

41. Arrabal, R.; Matykina, E.; Viejo, F.; Skeldon, P.; Thompson, G. Corrosion resistance of WE43 and AZ91D magnesium alloys with phosphate PEO coatings. *Corros. Sci.* **2008**, *50*, 1744–1752. [CrossRef]

42. Jin, W.; Wu, G.; Gao, A.; Feng, H.; Peng, X.; Chu, P.K. Hafnium-implanted WE43 magnesium alloy for enhanced corrosion protection and biocompatibility. *Surf. Coat. Technol.* **2016**, *306*, 11–15. [CrossRef]